Geoscience Frontiers 10 (2019) 753–767

HOSTED BY

Contents lists available at ScienceDirect

China University of Geosciences (Beijing)

Geoscience Frontiers

journal homepage: www.elsevier.com/locate/gsf

Research Paper

Evaluation of potential landslide damming: Case study of Urni landslide, Kinnaur, Satluj valley, India

Vipin Kumar [a], Vikram Gupta [a,*], Imlirenla Jamir [a], Shovan Lal Chattoraj [b]

[a] Wadia Institute of Himalayan Geology, 33 GMS Road, Dehradun, Uttarakhand, 248001, India
[b] Indian Institute of Remote Sensing, 4, Kalidas Road, Dehradun, Uttarakhand, 248001, India

ARTICLE INFO

Article history:
Received 19 September 2017
Received in revised form
9 March 2018
Accepted 1 May 2018
Available online 26 May 2018
Handling Editor: E. Shaji

Keywords:
Urni landslide
Slope stability
Rainfall
Landslide damming
Satluj valley

ABSTRACT

This work aims to understand the process of potential landslide damming using slope failure mechanism, dam dimension and dam stability evaluation. The Urni landslide, situated on the right bank of the Satluj River, Himachal Pradesh (India) is taken as the case study. The Urni landslide has evolved into a complex landslide in the last two decade (2000–2016) and has dammed the Satluj River partially since year 2013, damaging ~200 m stretch of the National Highway (NH-05). The crown of the landslide exists at an altitude of ~2180–2190 m above msl, close to the Urni village that has a human population of about 500. The high resolution imagery shows ~50 m long landslide scarp and ~100 m long transverse cracks in the detached mass that implies potential for further slope failure movement. Further analysis shows that the landslide has attained an areal increase of 103,900 ± 1142 m^2 during year 2004–2016. About 86% of this areal increase occurred since year 2013. Abrupt increase in the annual mean rainfall is also observed since the year 2013. The extreme rainfall in the June, 2013; 11 June (~100 mm) and 16 June (~115 mm), are considered to be responsible for the slope failure in the Urni landslide that has partially dammed the river. The finite element modelling (FEM) based slope stability analysis revealed the shear strain in the order of 0.0–0.16 with 0.0–0.6 m total displacement in the detachment zone. Further, kinematic analysis indicated planar and wedge failure condition in the jointed rockmass. The debris flow runout simulation of the detached mass in the landslide showed a velocity of ~25 m/s with a flow height of ~15 m while it (debris flow) reaches the valley floor. Finally, it is also estimated that further slope failure may detach as much as 0.80 ± 0.32 million m^3 mass that will completely dam the river to a height of 76 ± 30 m above the river bed.

1. Introduction

The landslide damming is a normal geomorphic process in the narrow river valleys (Evans et al., 2011) and is common in the mountainous environment (Costa and Schuster, 1991). Such damming may last for days to years before breaching, depending upon the dam dimension, dam material, stream power, upstream catchment area and valley width (Li et al., 1986; Costa and Schuster, 1988). These landslide dams may be classified as either partial (not formed) or complete (stable or unstable) and usually result in impounding of lakes, landslide lake outburst flood (LLOF), secondary landslides, channel avulsion and formation of flood terraces in the downstream region (Ruiz-Villanueva et al., 2016; Stefanelli et al., 2016). The most disastrous outcome of such dams is LLOF that greatly affects the downstream community and infrastructure (Dai et al., 2005; Gupta and Sah, 2008; Delaney and Evans, 2015). Previous studies have shown that the complex landslides dam the river most frequently and rainfall storms are most influential trigger for these events (Costa and Schuster, 1988). However, damming of rivers by the debris flow has also been reported (DeGraff and Rogers, 2003) and these debris flow events are equally catastrophic as the LLOF (Larsen and Wieczorek, 2006; Ray et al., 2016). The spatio-temporal variation in climate and seismically active nature of the Himalaya make the river valleys more prone to landslides that often create such landslide dams (Singh et al., 1974; Sundriyal et al., 2007; Gupta and Sah, 2008; Parvaiz et al., 2012). Further, the risk posed by such events has been aggravated during the recent years in the Himalaya (Schwanghart et al., 2016).

* Corresponding author.
E-mail address: vgupta@wihg.res.in (V. Gupta).
Peer-review under responsibility of China University of Geosciences (Beijing).

https://doi.org/10.1016/j.gsf.2018.05.004

Presently, there are many methods for the evaluation of damming process that are based on, geomorphic indices (Costa and Schuster, 1988; Ermini and Casagli, 2003; Stefanelli et al., 2016), hydraulic approaches (Takahashi and Nakagawa, 1993; Fujisawa et al., 2009) and velocity measurement of dam material (Wang et al., 2016). However, uncertainty still exists in evaluating the potential damming and assessment of the associated risk that can be narrowed down by understanding (i) pre-dam formation mechanism, (ii) dam dimensional characteristics and (iii) dam stability evaluation. Slope stability analysis and landslide triggering factors can be considered to constitute the pre-dam formation process, whereas dam dimension is controlled by the landslide volume and valley geometry (Canuti et al., 1998). In general, discontinuum modelling has been in practice for rock slope stability (Kainthola et al., 2015). However, continuum modelling (e.g., finite element method) is widely used for debris as well as rock slope stability analysis owing to its flexibility to incorporate material variability and complex slope geometry (Pain et al., 2014; Gupta et al., 2016a; Jamir et al., 2017; Kumar et al., 2018a). To evaluate the dam stability, global dataset based geomorphic indices that involve dam as well as valley characteristics have been used recently in different mountainous environments (Ermini and Casagli, 2003; Stefanelli et al., 2016). Grain size variability of the landslide material has also been noted to control the dam stability (Dunning and Armitage, 2011).

This work presents an evaluation of the potential landslide dam using satellite imagery to decipher the spatio-temporal changes in the landslide; satellite based rainfall data to understand triggering process; finite element modelling (FEM) for slope stability analysis and Voellmy model (Voellmy, 1955) for debris flow simulation. A new half ellipsoidal approach is used to determine the dimension of potential dam. Geomorphic indices, grain size data, and geological considerations are used to assess the dam stability. The Urni landslide, Kinnaur, Himachal Pradesh (India), situated along the right bank of the Satluj River is taken as the case study site. The landslide was initially of rockfall type during 1990s (Gupta, 2005) that, however, has evolved into a 'complex' landslide involving both rockfall and debris slide. The landslide has also partially dammed the Satluj River since 2013 and henceforth is subjected to frequent slope failures since then. The exact date of damming is still unknown. Therefore, considering the urgent need of disaster risk reduction in this remote tribal area, an attempt is made to evaluate the possibility of complete damming. The limitations and assumptions of the methodology are also further discussed.

2. Study area

The Urni landslide is ~600 m long and ~300 m wide and is located at lattitude 31°31′15″N and longitude 78°07′34″E along the Satluj River, Kinnaur district, Himachal Pradesh (Fig. 1). The crown

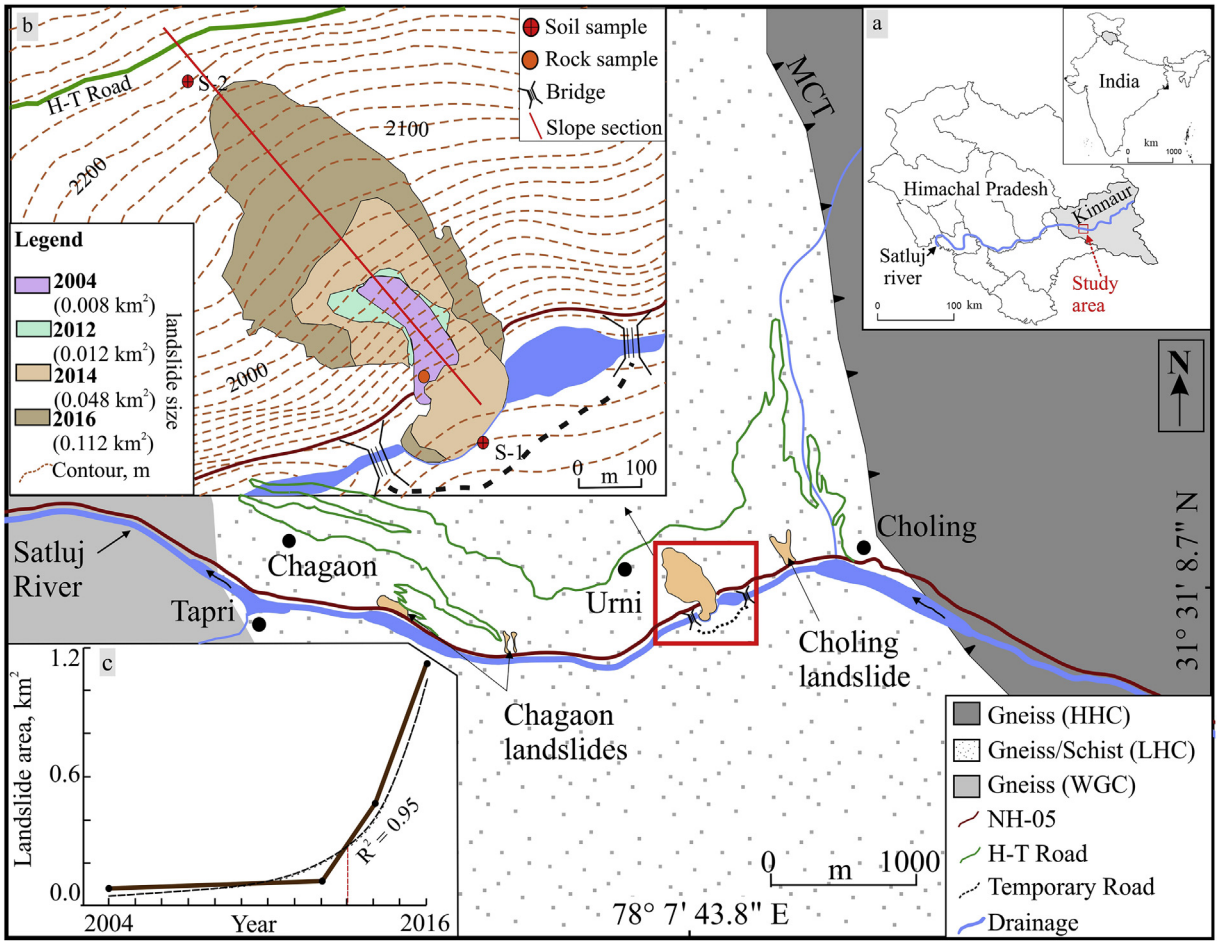

Figure 1. Study area map. Insert: (a) position of study area in the Kinnaur region (India); (b) enlarged view of the Urni landslide depicting spatio-temporal changes; (c) increase in the landslide area during yrs. 2004–2016. Acronym NH and H-T refer to National Highway and Hindustan-Tibet, respectively. Geological setting is based on Sharma (1977), Srikantia and Bhargava (1998), Vannay et al. (2004) and our own field observation. HHC, MCT, LHC and WGC refer to Higher Himalaya Crystalline, Main Central Thrust, Lesser Himalaya Crystalline and Wangtu Gneiss Complex.

portion of the landslide is arcuate in shape and located at elevation ranging between 2180 and 2190 m above mean sea level (msl). The landslide is of 'complex' nature (Cruden and Varnes, 1996) as it comprises rockfall at both the flanks and debris slide in the central part. The Urni village is located near the crown portion of landslide at altitudinal range of 2260–2300 m above msl. The village has a human population of ~500 (Chandramouli, 2011). Choling, Tapri, and Chagaon villages are located in the vicinity of the landslide. The landslide has damaged ~200 m stretch of the National Highway (NH)-05 and partially dammed the Satluj River in the narrow ('V' shaped) valley since the year 2013 (Fig. 2). The NH-05 passes through the toe portion of the landslide at an elevation of ~1820 m above msl. Based on the satellite imagery and field observation, the area of landslide is divided into 3 categories; detachment zone (Dt), transportation zone (Tr), and deposition zone (Dp). Deposition zone is further classified into deposition on slope (Dp_s) and deposition on river bed (Dp_r) (Fig. 3). The existing instability features in the landslide slope include ~100 m long transverse cracks in the detachment zone (Dt) and ~50 m long landslide scarp near the crown (Fig. 3). These transverse cracks are minor scarps on the detached landslide mass and its (detached mass) thickness varies from 5 to 15 m. This thickness estimation is based on field observation and information from local villagers. The Urni landslide hillslope is constituted by gneissic rockmass that belongs to the Lesser Himalaya Crystalline (Berthelsen, 1951; Sharma, 1977; Gupta, 2005). The slopes in the vicinity of landslides are steep (65°–70°) and sparsely vegetated by shrubs. The rockmass exposed on the landslide flanks comprises three set of joints (J1, J2, and J3). These trend NNW–SSE, NW–SE and ENE–WSW dipping at angle of 20°, 60° and 65°, respectively (Fig. 2a). The opposite slope of the landslide also consists of highly weathered and blocky gneissic rockmass that is prone to rockfall (Fig. 2f). The region exists in the

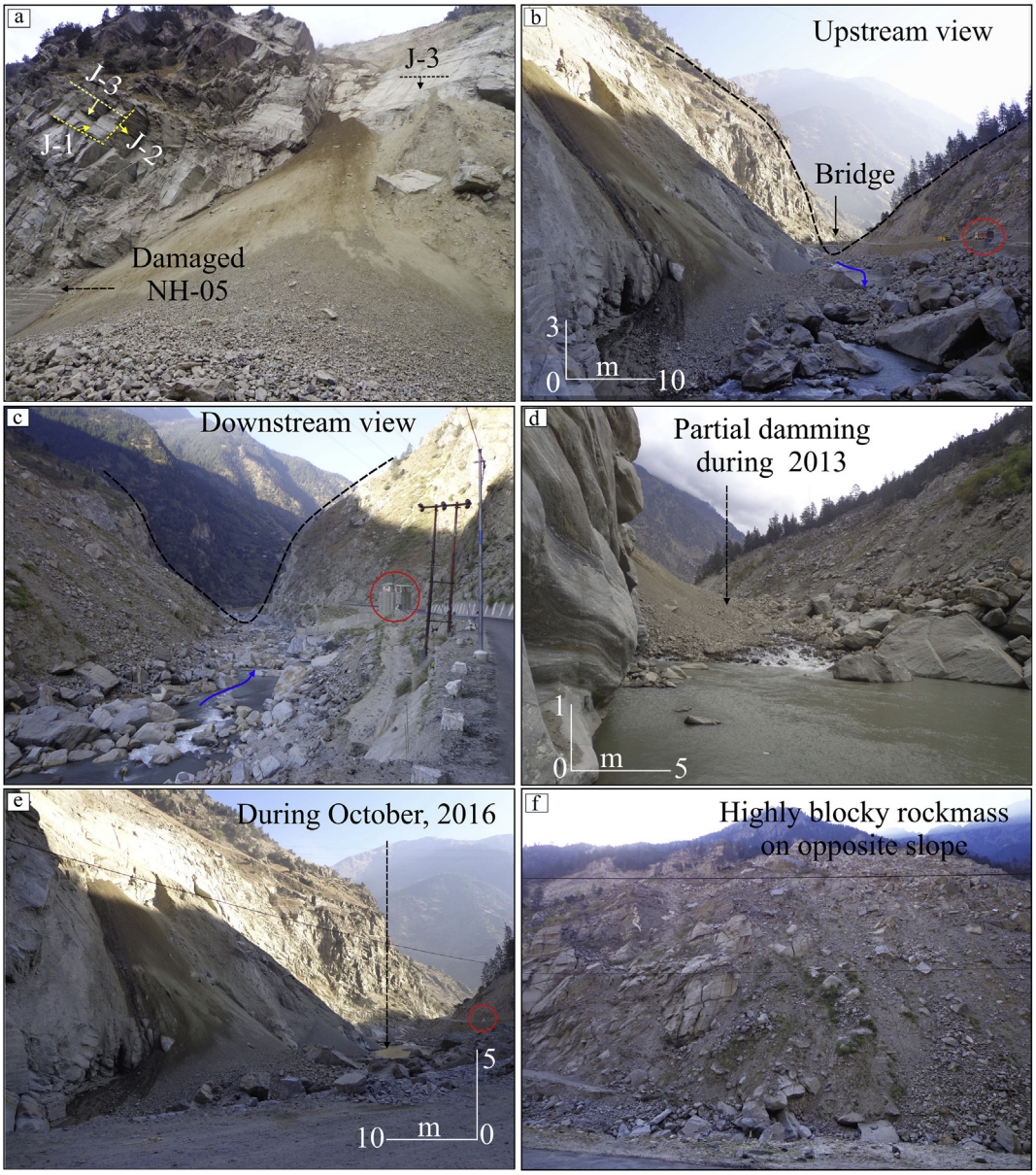

Figure 2. Field photographs. (a) Front face of the landslide; (b) and (c) are upstream and downstream view of the valley from the landslide location; (d) and (e) denote river damming during year 2013 and 2016, respectively; (f) slope in the opposite side. Red circles denote relative size by encircling heavy truck (~5 m × 2.5 m × 2.5 m) in 2b, 2e and tunnel outlet building (~6 m × 4 m) in 2c.

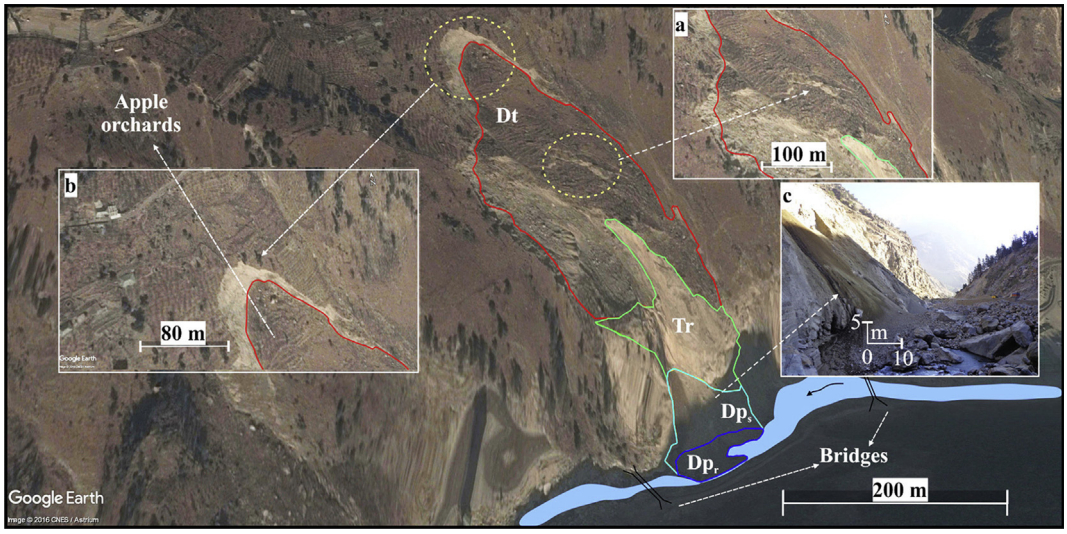

Figure 3. Deformation pattern in the different parts of the landslide and partial damming of the river. (a) ~100 m long transverse cracks in the detached mass; (b) ~50 m long landslide scarp. Affected agricultural land (apple orchards) is also visible; (c) ~5–10 m thick landslide debris in the zone of deposition. The 'Dt', 'Tr', 'Dp_s' and 'Dp_r' are detachment zone, transportation zone, deposition on slope and deposition on the river bed, respectively.

frontal part of the Higher Himalayan orographic barrier (Wulf et al., 2010; Kumar et al. 2018b) and receives maximum rainfall during summer monsoon season (June–September).

3. Methodology

The methodology adopted is presented in Fig. 4 and is briefly described hereunder.

3.1. Pre-dam formation

The high resolution (~1.5 m) Google Earth (GE) imagery (Fisher et al., 2012) was used to determine the spatio-temporal evolution of the landslide. Table 1 lists the details of the satellite imageries used in the analyses. The uncertainty (error) in the landslide dimension caused by measurement in the GE was determined by comparing the known distance of Survey of India toposheet 53/I/2 with the

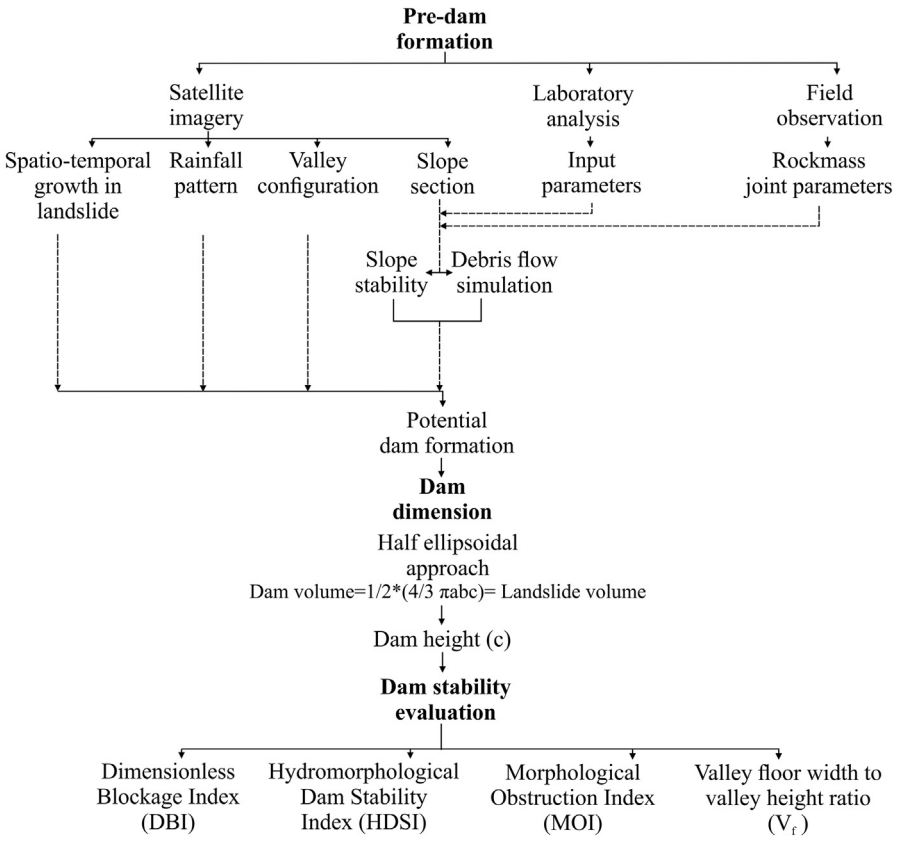

Figure 4. Flow chart of the methodology.

Table 1
Details of the satellite imageries used in the study.

Satellite data used	Date of data	Resolution	Purpose
Google Earth Imagery[a]	21st Nov. 2004 2nd Nov. 2012 10th Oct. 2014 30th Dec. 2016	~1.5 m	Spatio-temporal mapping of the landslide

[a] Google does not make public the specific type of the imagery used in Google Earth. However, approximate resolution of Google Earth in field is 0.5–2.5 m. Fisher et al. (2012) have related this level of resolution to Worldview-1, 2, and Quickbird imagery (DigitalGlobe, Inc.).

Table 2
Results of the grain size analysis.

Sample location	S-1 (at deposition zone)	S-2 (near landslide crown)
Textural group[a]	Sandy gravel	Gravelly sand
Sample type[a]	Bimodal, poorly sorted	Unimodal, poorly sorted
Mean[b]	730.6 μm	701.9 μm
Median	680.9 μm	471.4 μm
Sorting	1102.4 μm	653.0 μm
Skewness	1.69 μm (very fine skewed)	1.45 μm (symmetrical)

[a] Folk and Ward, 1957.
[b] Mean, median, sorting and skewness were calculated using arithmetic Method of Moments in GRADISTAT v.8 (2010).

same distance in the GE imagery. A difference of 1.06% was determined between known distances (from toposheets) and measured ones in the GE. This difference is used as the error in the final dimensional statistics of the landslide. Similar procedure has also been used by Mohammed et al. (2013) and Kumar et al. (2018b).

The LISS-IV and Cartosat-1 stereopair images were used to prepare the Digital Elevation Model (DEM) that was used to extract the slope geometry of the landslide (Fig. 5). Two soil samples (S-1 and S-2) and one rock sample, collected from the landslide location (Fig. 1) were analysed in the Wadia Institute of Himalayan Geology (WIHG) laboratory. S-1 was collected from the zone of deposition, whereas S-2 was collected near the crown of the landslide. It is assumed that S-2 represents the soil type that is exposed in the landslide scarp in the detachment zone. The grain size analysis of the soil samples was carried out using the standard dry sieving method as per Indian Standards (IS): 2720-Part 4, 1985. Both the samples contain <5% fines (<75 mm) and hence hydrometer test was not performed for the remaining fine material. The grain size data was further analysed using software GRADISTAT (v.8), which revealed that S-1 sample is sandy gravel whereas S-2 is gravelly sand (Table 2). Cohesion (c) and angle of internal friction (ø) of the soil were determined using the direct shear test (IS: 2720-Part 13, 1986). The samples were sheared under constant normal stress of 50, 100 and 150 kN/m^2. The Young's modulus of soil was measured by uniaxial compressive strength (UCS) test using three different rate of movements i.e., 1.25 mm/min, 1.50 mm/min and 2.5 mm/min (IS: 2720-Part 10, 1991). Poisson's ratio of 0.4 was taken as a standard value for the gravelly sand soil (Bowles, 1996). Seismic velocities (both P- and S-waves) of rock samples were measured using CATS Ultrasonic (1.95) of Geotechnical Consulting & Testing Systems (GCTS) to determine the density, Young's modulus, and Poisson's ratio of gneissic rock sample. The UCS of rock was determined as per IS: 9143, 1979.

The rockmass joints (J1, J2, and J3), mapped in the field were incorporated in the slope model for slope stability analysis (Fig. 5). The value of joint orientation, joint filling, Geological Strength Index (GSI), Joint Roughness Coefficient (JRC), and Joint Compressive Strength (JCS) are mentioned in Table 3. These joint properties were used in Barton and Bandis (1990) criteria. Further joint details and criteria used in the slope stability analysis are presented in Table 4. The peak and residual GSI values were determined using GSI based method, proposed by Cai et al. (2007). The JRC values, ranging from 4 to 8 were determined using the chart proposed by Barton and Choubey (1977). The Schimdt hammer (L type) values of the rockmass ranged from 45 to 55 and hence JCS value of 90–130 MPa were determined using the empirical chart of Deere and Miller (1966). Considering the influence of scale on JRC and JCS, scale corrected JRC$_n$ and JCS$_n$ were calculated using Barton and Bandis (1982) criteria. The value of reduced friction angle is taken in a range of 26°–34° considering joint filling and rock type (Barton, 1973). Considering the possible uncertainty caused by arbitrary selection of parameters (Hogg and Craig, 1995), final values of JRC$_n$,

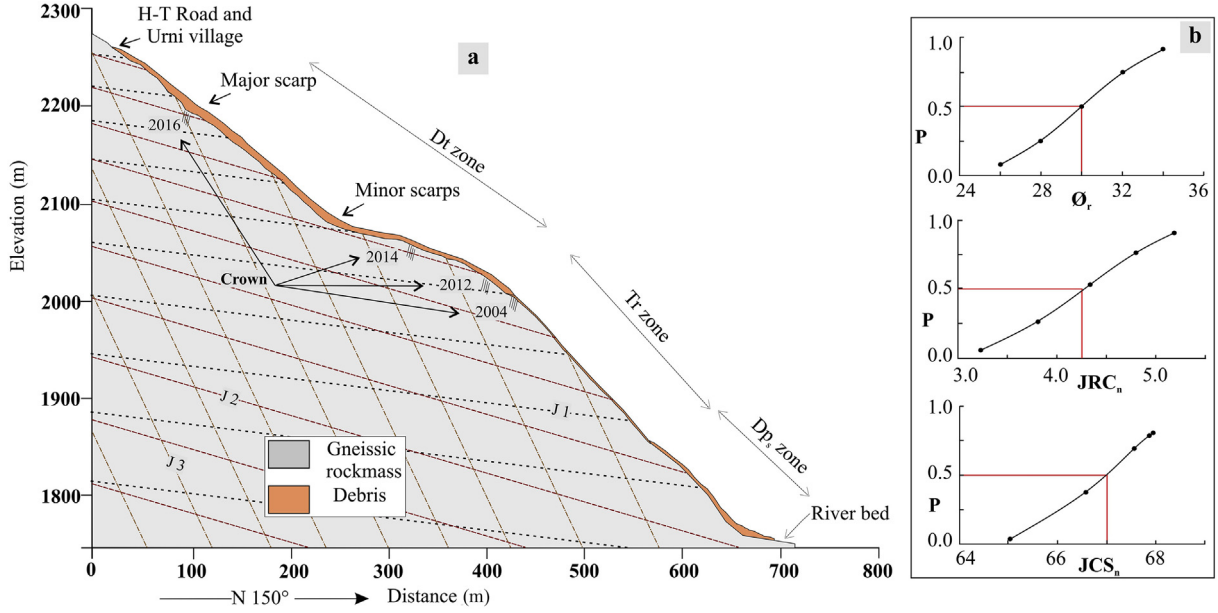

Figure 5. Slope outline and criteria. (a) Model configuration. Joint spacing is not to scale; (b) normal distribution of ø$_r$, JRC$_n$, and JCS$_n$. Red line marks the value of these parameters at 50% probability (P).

Table 3
Joint mapping data.

Parameter		J1	J2	J3
Dip amount/Dip direction		20°/70°N	60°/220°N	65°/160°N
Insitu block size, L_n (m)		1.5	1.0	0.75
Joint filling		*Sandy/rock fragments*		
Residual friction angle, $ø_r$ (°)		26	26	26
		28	28	28
		30	30	30
		32	32	32
		34	34	34
Geological Strength Index (GSI)		40 (Residual) -50 (Peak)		
Joint Roughness Coefficient (JRC)	Field based JRC	4	4	4
		5	5	5
		6	6	6
		7	7	7
		8	8	8
	Scale corrected JRC_n	3.22	3.33	3.40
		3.81	3.97	4.09
		4.34	4.55	4.71
		4.79	5.07	5.28
		5.19	5.53	5.80
Joint Compressive Strength (JCS)	Field based JCS	90	90	90
		100	100	100
		110	110	110
		120	120	120
		130	130	130
	Scale corrected JCS_n	65.03	68.27	70.67
		66.62	70.79	73.92
		67.56	72.68	76.54
		67.95	73.99	78.60
		67.87	74.81	80.15

JCS_n and reduced friction angle values were selected at 50% probability from the normal distribution chart (Fig. 5). Joint stiffness (k_n and k_s) were determined using the stiffness criteria of Barton (1973) and rockmass modulus concept of Hoek et al. (2002). Details of the parameters are mentioned in Table 4.

The soil, rock, and joint parameters were further used for the FEM based slope stability analysis using Phase^2 (v.6) software. Shear strength reduction technique (Zienkiewicz et al., 1975; Matsui and San, 1992) was used to determine the Factor of Safety (FOS) of the slope. The boundary condition with restraining movement ($X = Y = 0$) was applied to the base and back of the model, whereas the front face of the model was kept free for movement The joints are considered as the interface in this continuum (FEM) modelling technique that has been used widely in rock slope stability studies (Pain et al., 2014; Xu et al., 2015). Elastic-perfectly plastic material model with Mohr-Coulomb strength criteria was used for the soil, whereas for rockmass, Generalized Hoek-Brown (GHB) criteria along with peak and residual parameters was used (Griffiths and Lane, 1999; Hoek et al., 2002; Cai et al., 2007; Gupta et al., 2016a; Jamir et al., 2017). The GHB parameters are mainly controlled by Geological Strength Index (GSI) that defines the degree of blocky nature and condition of discontinuity in the rockmass (Marinos et al., 2005). These parameters are mentioned in Table 3. Field stress was adjusted assuming a horizontal (σ_h) to vertical stress (σ_v) ratio of 0.5 (i.e. $k = \sigma_h/\sigma_v = 0.5$). The $k = 0.5$ was used considering extensional regime in the study area as inferred by Vannay et al. (2004). Similar value of k has also been used earlier in the extensional regime by Eberhardt et al. (2004). The final FEM model consisted of 3789 triangular elements (6 noded) in graded mesh. Using joint orientation data (Table 3), stereoplot based kinematic analysis was also performed. Kinematic analysis shows the possible failure direction and modes in a jointed rock mass by utilizing angular relationship between discontinuities and slope surfaces (Hoek and Bray, 1981).

Since, there is no rain-gauge station in the vicinity of the landslide region, daily rainfall data of 0.25° × 0.25° spatial resolution of the Tropical Rainfall Measuring Mission (TRMM_3B42RT) was extracted from Giovanni 4.21 data portal of the NASA. This data was used to understand the temporal (annual and monsoonal) pattern of the rainfall in the study area for the year 2000 to 2016. Further, envisaging the possibility of rainfall triggered debris flow, runout analysis was also carried out using RAMMS debris flow software (v.1.6). Precipitation triggered debris flow models have been attempted earlier also in similar environment (Chattoraj and Champatiray, 2015; Ray et al., 2016). The RAMMS debris flow model uses the Voellmy friction law (Voellmy, 1955) that divides the frictional resistance into two parts: dry-Coulomb type friction (μ) that scales with the normal stress and velocity-squared drag or viscous-turbulent friction (coefficient, ξ). The total frictional resistance S (kPa) is then:

$$S = \mu\rho Hg\cos(Ø) + \left(\rho gU^2\right)/\xi \quad (1)$$

where μ, friction coefficient; ρ, debris density (kg/m^3); H, release height (m); g, acceleration due to gravity (m/s^2); Ø, slope angle (°); U, flow velocity (m/s); ξ, drag coefficient (m/s^2). The main difficulty in such flow simulation is the much larger variety of debris flow materials that influence the choice of the friction parameters (Ray et al., 2016). It is quite possible that different events in the same torrent may show differences in composition. This fact makes the calibration of the friction parameters much more difficult. Therefore, number of simulations with different values for each input parameters were carried out to get desired results. Simulation output requires verification with previously modelled event as a part of validation strategy. However, validation was not possible since no such previous study has been carried out in this area. To determine the optimal friction value, a range of values were used. The friction coefficient ranges from 0.05 to 0.2 and drag coefficient

Table 4
Input parameters and criteria for the FEM based slope stability analysis.

Material criteria			Material value	
			Parameters	Value
Gneiss	Generalized Hoek & Brown (GHB) Criteria (Hoek et al., 2002) $\sigma_1 = \sigma_3 + \sigma_{ci}[m_b(\sigma_3/\sigma_{ci}) + s]$-$a$ $m_b = m_i e^{[(GSI-100)/(28-14D)]}$ $s = e^{[(GSI-100)/(9-3D)]}$ $a = \frac{1}{2} + \frac{1}{6}\left[e^{\left[-\left(\frac{GSI}{15}\right)\right]} - e^{\left[-\left(\frac{20}{3}\right)\right]}\right]$ GSI: Geological Strength Index (Cai et al., 2007) σ_{ci}: Compressive strength of intact rock D: Disturbance (dilation) factor, m_i: Intact rock property		Unit weight (MN/m^3)	0.027
			Young's Modulus (E_i), MPa	21,500
			Poisson ratio	0.3
			Uniaxial Compressive Strength (σ_{ci}), MPa	98
			Peak Geological Strength Index	50
			Residual Geological Strength Index	40
			Material constant (m_i) GHB parameters	25
			m_b (peak)	4.298
			m_b (residual)	2.899
			s (peak)	0.00418
			s (residual)	0.00122
			a (peak)	0.505
			a (residual)	0.512
			D (peak)	0
			D (residual)	0
Joint	Barton-Bandis Criteria (Barton and Bandis, 1990) $\tau = \sigma_n \tan[\phi_r + JRC\log_{10}(JCS/\sigma_n)]$ Here, τ: Joint shear strength, σ_n: Normal stress across joint, $\varnothing_r$: Reduced friction angle (Barton, 1973), JRC: Joint roughness coefficient, JCS: Joint compressive strength Joint Stiffness criteria (Barton, 1973) $k_n = (Ei^*Em)/L^*(E_i - E_m)$ Here, k_n: Normal stiffness, E_i: Intact rock modulus, E_m: Rockmass modulus L; Mean joint spacing = insitu block size E_m (GPa) = $(1-D/2)^*(\sigma_{ci}/100)^{0.5*(10^{(GSI-10)/40})}$ Hoek et al., 2002	J1	Normal Stiffness (k_n), GPa/m	12.2
			Shear Stiffness (k_s), GPa/m	1.22
			$\varnothing_r$	30
			Scale corrected JRC_n	4.25
			Scale corrected JCS_n, MPa	67
		J2	Normal Stiffness (k_n), GPa/m	18.3
			Shear Stiffness (k_s), GPa/m	1.83
			$\varnothing_r$	30
			Scale corrected JRC_n	4.5
			Scale corrected JCS_n, MPa	72.2
		J3	Normal Stiffness (k_n), GPa/m	24.4
			Shear Stiffness (k_s), GPa/m	2.44
			$\varnothing_r$	30
			Scale corrected JRC_n	4.6
			Scale corrected JCS_n, MPa	76
Gravelly sand	Mohr-Coulomb Criteria $\tau = C + \sigma\tan\varnothing$		Unit weight (MN/m^3)	0.019
			Cohesion, C (MPa)	0.01
			Angle of friction, Ø (Degree)	33
			Young's Modulus (MPa)	40
			Poisson ratio	0.4

ranges from 100 to 2000 m/s^2 (Sosio et al., 2008). Meanwhile other input parameters viz. density of material, release height, earth pressure coefficient and the percent of momentum were eventually kept constant. Afterward, validation of simulation outputs was done comparing the total length of run-out distance and the areal extend of run out vis-a vis the actual flow paths on ground. Input parameters and material criteria for the runout analysis are presented in Table 5.

3.2. Dam dimension

Based on the instability features of the landslide, it is highly probable to consider further slope failure movement that, if happened, may detach the slope material and eventually dam the river completely. To determine the possible dimension of such dam, a new conceptual approach is utilized. The 'V' shaped narrow valley region is best represented by half-ellipsoidal space and in case of slope failure, debris material would be deposited in it, until washed out by the fluvial action (Fig. 6). It has been observed that the dam volume in general remains equal to the landslide volume (Canuti et al., 1998), hence the detachable volume of the Urni landslide is kept equal to the volume of half ellipsoid. Thus:

$$landslide\ volume = Dam\ volume = \frac{1}{2}\left(\frac{4}{3}\right)\pi abc \quad (2)$$

Table 5
Input parameters and criteria for the debris flow simulation.

Criteria	Parameters	Value
Voellmy-fluid friction model (Voellmy, 1955)	Constant density (ρ), kg/m^3	2300
	Release height (H) or (debris thickness in Dt zone), m	10
$S = \mu\rho Hg\cos\text{Ø} + (\rho gU^2)/\xi$	Friction coefficient (μ)	0.1
S = frictional resistance, kPa	Drag coefficient (ξ), m/s^2	500
M = Friction coefficient		
ρ = Constant density, kg/m^3		
H = Release height, m		
g = Acceleration due to gravity, m/s^2		
Ø = Slope angle		
U = Flow velocity, m/s		
ξ = Drag coefficient, m/s^2		

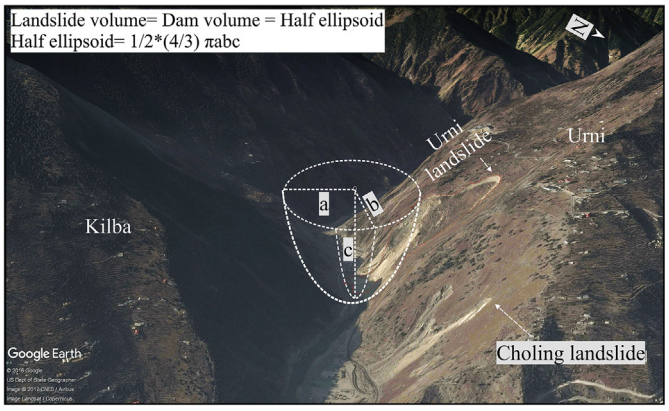

Figure 6. Dam dimension estimation using half ellipsoidal approach. Axis *a*, *b* and *c* of the half ellipsoid are ½ of the dam length, ½ of the dam width and dam height, respectively.

where, *a*, *b* and *c* are the axis of half ellipsoid and represent half of the dam length, half of the dam width and dam height, respectively. Different combinations of axis '*a*' and '*b*' are used in conjunction with field conditions to determine the height of the potential dam.

Studies have noted inequality in landslide and dam volume as final volume of dam may be lower (Dong et al., 2011) or higher (Hungr and Evans, 2004) than the landslide volume depending upon substrate entrainment, fragmentation of rockmass and/or remaining material on slope, and washout of landslide material by the river. However, due to potential character of landslide dam and considering the worst case scenario, dam volume is assumed to be equal to landslide volume (Eq. (2)). The volume of landslide mainly consists of debris volume in detachment zone (Dt), transportation zone (Tr), and deposition zone (Dp_s) (Fig. 3). The area of different zones was obtained by mapping their boundary in high resolution imagery (Google Earth) through shape, tonal variation and association of different features on the slope. The debris accumulation of 5–10 m in the 'Dp_s' zone was ascertained in the field and thus a thickness of 7.5 m (avg. value) ± 2.0 m was used for volume calculation (Fig. 3c). The landslide debris resting over the river bed (in Dp_r zone) was not included in volume estimation of zone of deposition, considering the washout tendency of this material by the fluvial action. The GE satellite imagery and field observations were considered to deduce a thickness of 1–3 m in the 'Tr' zone and an average value of 2 ± 0.8 m was used for volume estimation. Debris thickness in 'Dt' zone may vary from 5 to 15 m and hence an average value of 10 ± 4.1 m was used to estimate the debris volume in 'Dt' zone. The uncertainty (±) in these thickness values is standard deviation. Thus, the total volume attained by the landslide is 0.80 ± 0.32 million m^3 (Table 6).

3.3. Dam stability evaluation

Considering the possibility of landslide dam formation in view of further slope failure, stability evaluation of the potential landslide dam is done using the following geomorphic indices;

1. Dimensionless Blockage Index (DBI) by Ermini and Casagli (2003).

$$DBI = \log(A_b \cdot H_d / V_d) \quad (3)$$

2. Morphological Obstruction Index (MOI) by Stefanelli et al. (2016).

$$MOI = \log(V_l / W_v) \quad (4)$$

3. Hydromorphological Dam Stability Index (HDSI) by Stefanelli et al. (2016).

$$HDSI = \log(V_l / A_b \cdot S) \quad (5)$$

where, $V_d = V_l$ is volume of the landslide (m^3); A_b is upstream catchment area (km^2); W_v is width of dammed valley (m); H_d is dam height (m) and S is local slope gradient of river channel (m/m).

The values of these parameters are mentioned in Table 7. DBI, MOI and HDSI were calculated using landslide volume of 0.80 ± 0.32 million m^3 (Table 6).

Since grain size composition and its variation are also noted to control the breaching and longevity of the landslide dams (Dunning and Armitage, 2011), grain size analysis of the soil samples was also performed. Geological conditions were also considered in context of dam stability, as these conditions influence the river channel gradient and valley configuration. Hence, ratio of valley floor width to valley height (V_f) (Bull and McFadden, 1977) was also computed using the following equation:

$$V_f = 2V_{fw} / \left[(E_{ld} - E_{sc}) + (E_{rd} - E_{sc}) \right] \quad (6)$$

here, V_{fw} is valley floor width; E_{sc} is valley floor elevation; E_{ld} and E_{rd} are left and right valley divides, respectively. These parameters were extracted from the Cartosat-1 DEM. Generally higher V_f values characterize broad, flat-floored valleys and lower V_f characterize 'V' shaped valleys. The 'V' shaped valleys are usually associated with areas undergoing rapid uplift and valley incision (Keller and Pinter, 2002).

4. Results

It is observed that the landslide has attained an areal growth of 103,900 ± 1142 m^2 from 8300 ± 91 m^2 in year 2004 to 112,200 ± 1234 m^2 in year 2016 in an exponential (R^2 = 0.95)

Table 6
Estimation of landslide volume.

Parameters		Detachment zone (Dt)	Transportation zone (Tr)	Deposition Zone	
				Deposition on slope (Dp_s)	Deposition on river bed[a] (Dp_r)
Debris thickness (overburden), m	Min.	5	1	5	2
	Avg.	10	2	7.5	3
	Max.	15	3	10	4
	Std. dv.	4.1	0.8	2.0	0.5
Area[b], m^2		71,500 ± 787	15,000 ± 165	8050 ± 89	5110 ± 56
Volume[c], million m^3 (area × thickness)		0.715 ± 0.29	0.030 ± 0.012	0.060 ± 0.017	0.015 ± 0.002
Total Volume, million m^3		(0.715 ± 0.29) + (0.030 ± 0.012) + (0.060 ± 0.017) = 0.80 ± 0.32			

[a] Debris on the river bed is prone to washout by the fluvial action. The thickness and area of this zone was noted during Oct. 2016 field observation. Considering its washout possibility by the river, it is not included in the total landslide volume which will contribute to the dam formation, in the event of slope failure.
[b] Error (±) in area corresponds to measurement error (1.06%) associated with Google Earth (Details in Methodology).
[c] Error (±) is an outcome of multiplication of area ± error and thickness ± error.

Table 7
Input parameters for geomorphic indices based dam stability evaluation.

Landslide volume ($V_d = V_l$), million m^3	Upstream catchment area (A_b), km^2	Width of dammed valley (W_v), m	Maximum Dam height (H_d), m	Local slope gradient (S)
0.80 ± 0.32	4490	60	76 ± 30	0.007

manner (Fig. 1). About 86% areal increase has occurred since year 2013. The individual zones in the landslide; Dt, Tr and Dp also changed in their longitudinal extent (along the slope) over this time period (Fig. 7). The 'Dt' zone attained 315 ± 3 m increase in its length from 77 ± 0.8 m in year 2004 to 392 ± 4.3 m in year 2016. The 'Tr' zone attained 8 ± 0.1 m increase, followed by 27 ± 0.3 m in the 'Dp' zone. This spatial increase in the landslide dimension was found more pronounced towards the landslide crown, since its position has moved ~200 m upslope from 2000 m above msl in the year 2004 to 2200 m above msl in the year 2016 (Fig. 1). Similar pattern of headward retreat has also been observed by Sajinkumar et al. (2017) in the Western Ghats of Kerala.

Slope stability analysis revealed a Factor of Safety (FOS) of 1.01 (Fig. 8). Maximum shear strain and total displacement are noted to be 0.00–0.16 and 0.0–0.6 m, respectively in the "Dt' zone. Kinematic analysis showed that jointed rockmass comprises wedge and planar failure condition (Fig. 8). The line of intersection of J2 and J3 joint plane plunges 58° towards 200°N, credential of wedge failure, while planar failure condition is satisfied by joint plane J3.

The annual rainfall trend during the year 2000–2016 showed an abrupt increase in rainfall in the year 2013 (Fig. 9a). The mean total annual rainfall attained ~42% increase from 1460 mm/yr during the year 2000–2012 to 2075 mm/yr during the year 2013–2016. The monsoon rainfall (June–September) is noted to account ~60% of the annual rainfall out of which maximum contribution is observed during July and a minimum during June (Fig. 9b). However, maximum uncertainty (standard error of mean) is also subjected to the month of July that reflects the high interannual variation in the precipitation. Notably, in the year 2013, there is a remarkable increase in the rainfall in June month (>550 mm) in comparison to the preceding years (Fig. 9c). This extreme rainfall in June 2013 was mainly contributed by ~100 mm at 11th day and 115 mm at 16th day (Fig. 9d).

The debris flow runout analysis showed that debris flow may hit the valley floor and temporary part of the NH-05 with a ~15 m high flow of ~25 m/s velocity (Fig. 10). The runout extent of debris flow along the river channel may be as high as ~500 m in the upstream and downstream direction.

Using the half ellipsoidal approach, it was found that the dam height is controlled by the dam length and dam width (Fig. 11). On increasing the '*a*' (1/2 of dam length) from 30 to 100 m and '*b*' (1/2 of dam width) from 100 to 200 m, *c* (dam height) diminishes. The following field conditions were taken into consideration to estimate the possible height of the landslide dam;

(1) Presently, the valley floor width is ~60 m (i.e., $a = 30$ m) and in case of further slope failure, landslide volume (0.80 ± 0.32

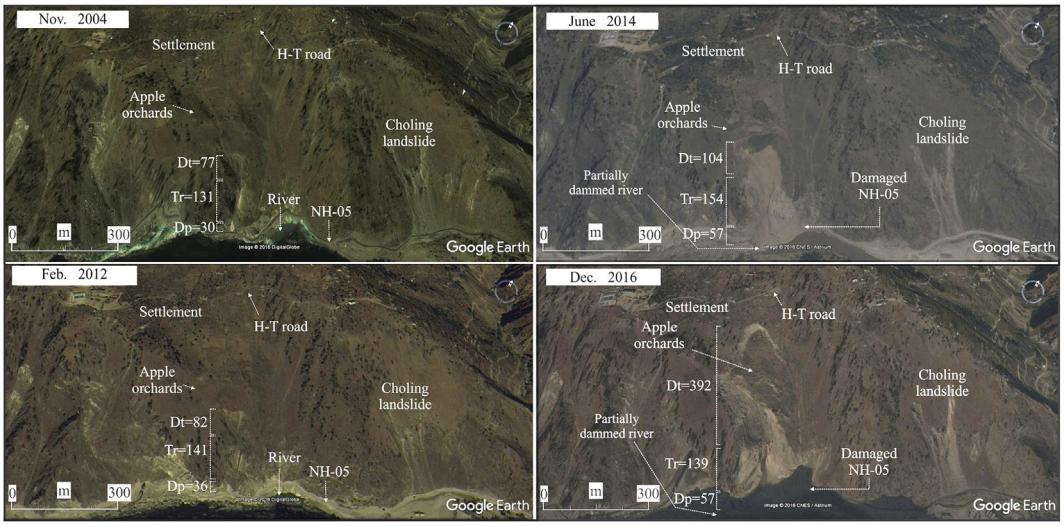

Figure 7. Spatio-temporal changes in the different zones of the landslide. The 'Dt', 'Tr' and 'Dp' correspond to the detachment, transportation and zone of deposition.

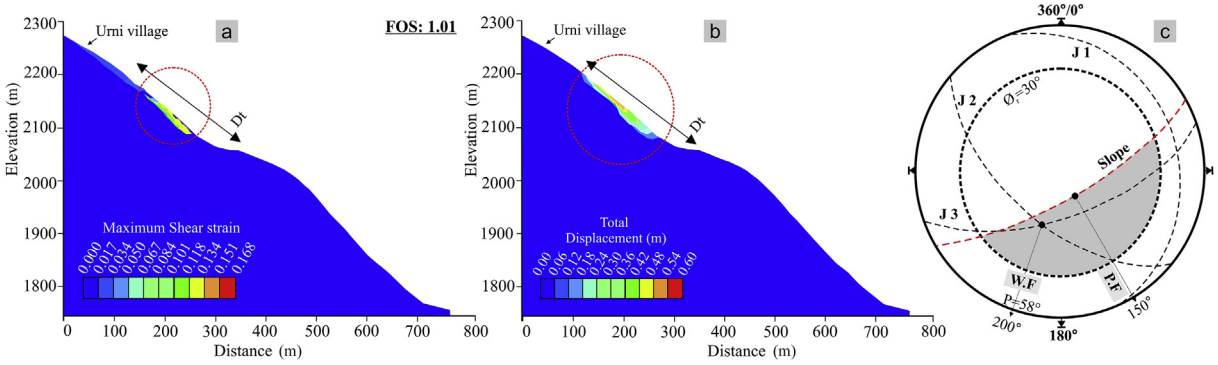

Figure 8. Results of the slope stability analysis. (a) and (b) correspond to the FEM based results; (c) kinematic analysis based output. The 'P.F' and 'W.F' denote planar and wedge failure, respectively. The 'P' represents plunge of line of intersection of J2 and J3 planes. J1, J2, J3 are joint planes. $ø_r$ refers to reduced friction angle.

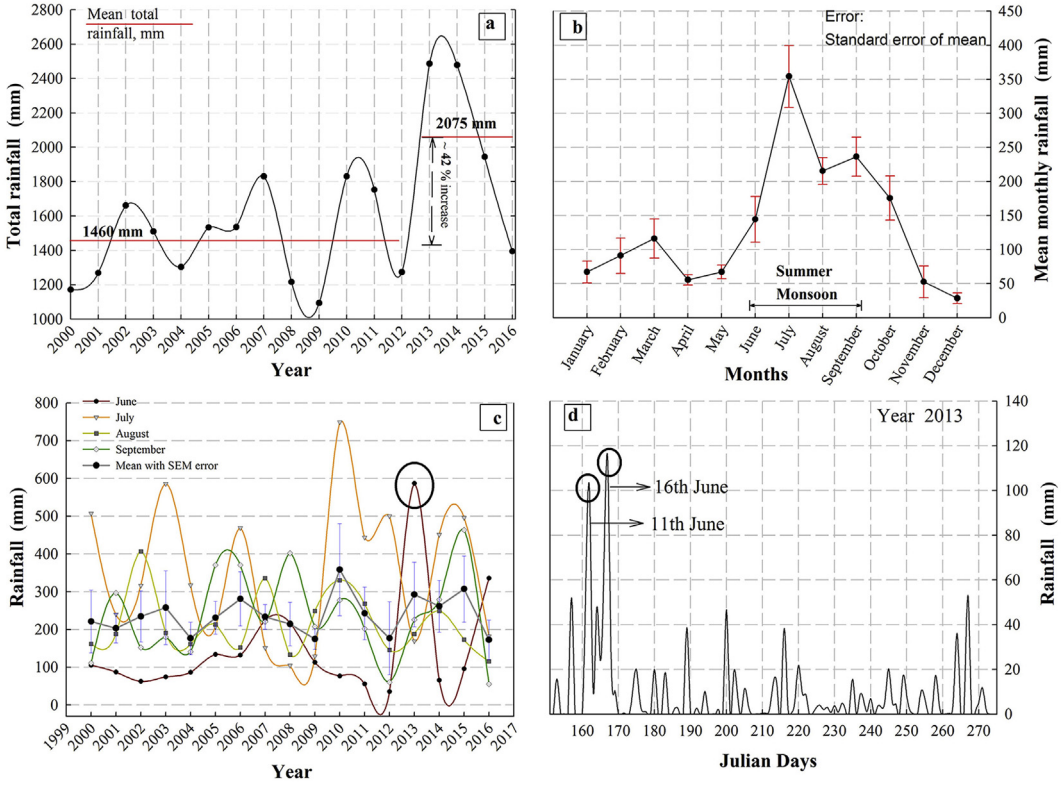

Figure 9. Rainfall pattern in the study area. (a) Annual variation in total rainfall (mm); (b) seasonal variation of mean monthly rainfall (mm) with standard error of mean (SEM); (c) annual rainfall variation during summer monsoon; (d) Julian day (June–September) variation in the rainfall (mm). Black circles in (c) and (d) show the extreme rainfall in the June, 2013 and on specific days, respectively.

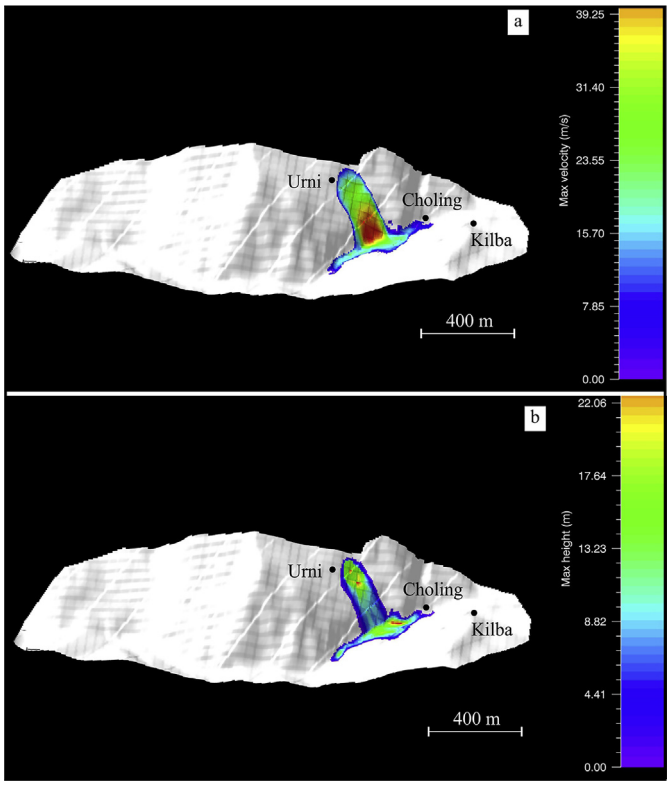

Figure 10. Debris flow simulation. (a) Maximum flow velocity; (b) maximum flow height.

million m^3) will cover this floor width and may extend beyond on the side hillslopes. This extent is marked by a red dash line in Fig. 11.

(2) The valley floor is partially dammed by the debris, accumulated from previous movements extending to ~15 m on side hillslopes. Therefore, on further slope failure, the '*a*' will be higher than 45 m (a+15 = 30 + 15) of the resulting dam. This condition is marked by a blue dash line in Fig. 11. Thus, this $a = 45$ m marks the lower limit of dam height estimation and $a = 120$ m is assumed to be the upper limit.

(3) The existing partial dam already extends ~ 200 m in width (Fig. 3) and release of landslide volume (0.80 ± 0.32 million m^3) may result in a width higher than this. Hence, we have considered '$b = 100$ m' (since $2b = 200$ m) as the lower limit of the dam width and only those values of b were considered for dam height estimation that are higher than 100 m.

In view of these field conditions, it was estimated that dam may attain a maximum height of 76 ± 30 m at landslide volume of 0.80 ± 0.32 million m^3. The uncertainty (±) in predicted dam height is caused by uncertainty in landslide volume. Dam height and associated uncertainties are found to decrease with increasing dam length and dam width.

The MOI index for the Urni landslide potential dam falls in the 'Formation domain' with error tail in 'Uncertain domain' (Fig. 12a). The Formation domain implies the possibility of dam formation in case of slope failure whereas uncertain domain suggests the possibility of 'Formation' as well as 'No-Formation'. The HDSI and DBI indices belonged to 'Instability domain' (Fig. 12b and c). The grain size analysis of the soil samples (S-1, S-2) showed poorly sorted sandy soil (Table 2). Further, valley attains a V_f ratio of 0.28 at the

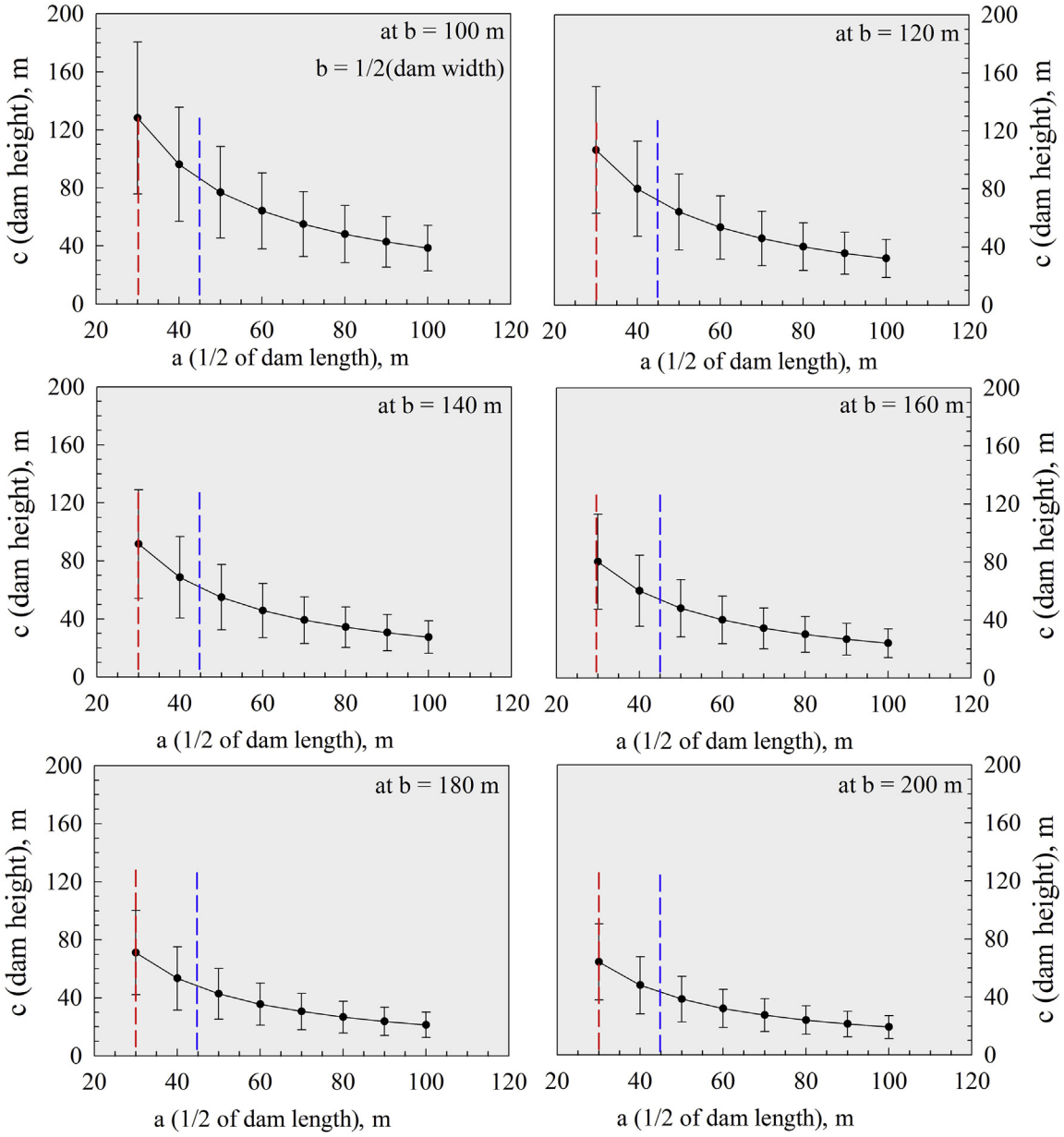

Figure 11. Dam height estimation chart. Red line shows the extent of valley width i.e., equal to 2a; whereas blue line indicates the current extent of debris on the side hillslopes.

location of Urni landslide (Fig. 12d) that is also coupled with a prominent knick point of the river channel. The Urni landslide exists in a deep gorge geomorphic setting (Fig. 2b and c) bounded by wide valley portions in upstream and downstream regions.

5. Discussion

The Urni landslide, that was a wedge failure type rockfall in year 1990s has evolved in last two decade (2000–2016) into a complex landslide, comprising debris slide in the central part and planar/wedge failure type rockfall at the flanks (Figs. 2a and 3). The landslide attained an areal increase of 103,900 ± 1142 m^2 during the year 2004–2016 and ~86% of this total increase occurred since year 2013. Notably, the similar change is also seen in the rainfall pattern that showed ~42% increase in mean annual rainfall since year 2013 (Fig. 9a). Further, seasonal and daily rainfall pattern revealed that the sudden increase in rainfall in the year 2013 was constituted primarily by two extreme rainfall events; 11th and 16th June (Fig. 9d). Such extreme rainfall events were also observed in other parts of the Northwest Himalaya that caused widespread landslides (Martha et al., 2015; Gupta et al., 2016b; Kumar et al., 2017). Therefore, we are of understanding that the increase in the landslide area, particularly since the year 2013 and the partial river damming since June, 2013 (www.timesofindia.com, retrieved on 12th August 2014; www.amarujala.com, retrieved on 14th June 2016) may pertain to such extreme rainfall events.

Further, based on the marginally stable condition (Zienkiewicz et al., 1975; Matsui and San, 1992) of the slope (FoS = 1.01) from FEM analysis, possibility of planar and wedge type failure from kinematic analysis (Fig. 8) and the observed surface instability features (Fig. 3), the possibility of further aggravation in slope failure cannot be ruled out. Therefore, in view of increasing annual rainfall and extreme rainfall events (Fig. 9), possibility of debris slide and/or debris flow strongly exists (Figs. 8 and 10). Both

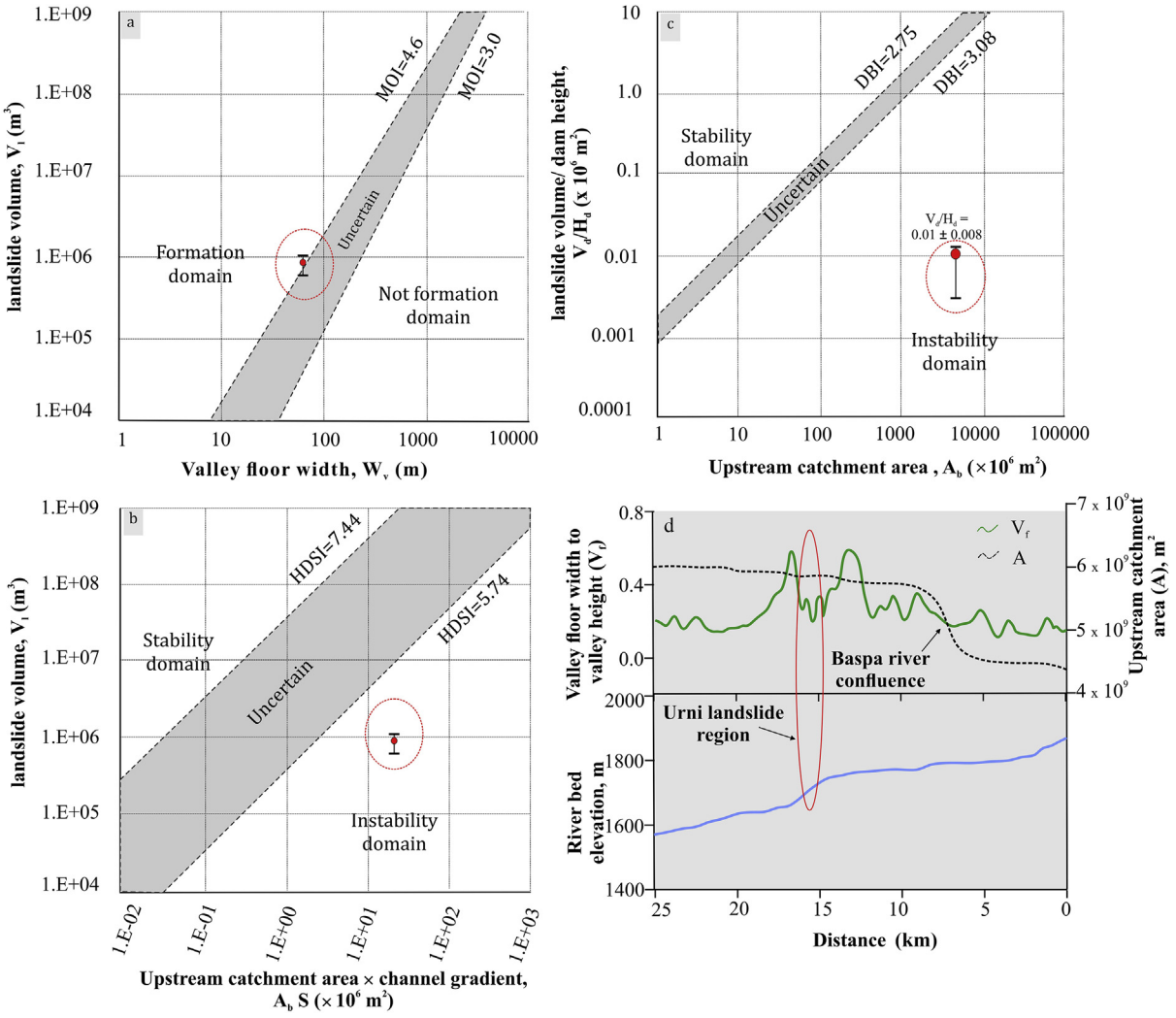

Figure 12. Stability evaluation of the potential dam. (a) Morphological Obstruction Index; (b) hydro-morphological Dam Stability Index; (c) dimensionless Blockage Index. The 'H_d' indicates dam height; (d) spatial variation of V_f ratio and upstream catchment area.

processes may detach as much as 0.80 ± 0.32 million m^3 debris onto the river channel and may dam the Satluj River completely. Case studies have shown that debris flows are equally catastrophic in damming as the complex landslides (Costa and Schuster, 1988; DeGraff and Rogers, 2003). Since, during debris flow simulation, side channel contribution and en-route erosion were not considered (Ray et al., 2016), flow parameters might achieve higher values in real scenario. In such case, the Urni village (~100 m upslope the landslide crown), Chooling village (~500 m upstream Urni landslide), two bridges (within ~100 m range of Urni landslide) worth ~0.6 million $, and vast part of the NH-05 may get severely affected by such debris flow. Thus, taking into account the areal growth of landslide, temporal increase in rainfall, slope instability, and potential debris flow in narrow valley confinement, there is great likelihood of dam formation. We observed that the potential Urni dam may achieve a maximum height of 76 ± 30 m at a landslide volume of 0.80 ± 0.32 million m^3 (Fig. 11). Exact dam height cannot be affirmed as it is controlled by dam length and width, that in turn depend upon the final landslide volume. The 76 ± 30 m dam height implies that the dam crest may reach ~76 m high from the present altitude of the river channel (i.e. ~1760 m above msl). The instant effect of this damming will include complete destruction of the NH-05 in this region and two bridges (worth ~0.6 million $), situated near the landslide (Fig. 1).

The geomorphic indices (MOI, HDSI, and DBI) indicated unstable tendency of the potential Urni landslide dam (Fig. 12). Low V_f ratio (~0.28) indicates narrow geomorphic setting which also implies that the region is tectonically active. Further, the study area exists in the vicinity of the Main Central Thrust (Fig. 1) and sustains high exhumation rate of ~2–4 mm/yr (Thiede et al., 2009). These tectonic implications make the region more prone to instability. The MOI, HDSI, and DBI indices, used by other workers also (Duman, 2009; Wang et al., 2016) cannot be ignored as the Satluj River has witnessed frequent outburst floods in the past (Gupta and Sah, 2008; Ruiz-Villanueva et al., 2016; Sharma et al., 2017). The recent six floods have claimed ~350 lives and loss of ~30 million US dollar (Ruiz-Villanueva et al., 2016). Further, Wulf et al. (2010) has quantified that Satluj River receives high sediment flux and peak discharge during summer season rainfall that in turn may raise the possibility of Urni landslide dam failure. However, the basic uncertainty in this 'outburst flood' proposition is subjected to the longevity of the dam. Study of historical events has shown a range of days to years for the breaching of landslide dams (Li et al., 1986; Korup, 2004; Ruiz-Villanuva et al., 2016; Stefanelli et al.,

2016). Such longevity, however, depends upon dam dimension, dam composition, and upstream drainage area (indicative of fluvial discharge). The maximum height of 76 ± 30 m may support the dam to stay longer in this narrow part of the valley. Nonetheless, it is also possible that the 'potential Urni landslide dam will not survive long due to poorly sorted sandy soil and huge upstream catchment area, since dams that are generally composed of poorly sorted, non-cohesive material and subjected to huge upstream drainage area may breach rapidly (Li et al., 1986; Swanson et al., 1986; Casagli et al., 2003; Dunning and Armitage, 2011). Thus, uncertainty is inevitable in ascertaining the breaching time due to various factors controlling this mechanism. Despite that, various mitigation measures including monitoring of Urni landslide and early warning system for downstream community are suggested because such dams and subsequent processes result in irreversible socio-economic loss.

5.1. Assumptions

(1) High resolution, multitemporal imagery in the GE are free, quick and easy to operate but require ground truthing. Random timing of images in the GE indicates that years of significant slope failure activity may not be present in the GE database. However, these imagery have been utilized widely in recent years due to shape, tonal and association contrast of the objects at high resolution (Blöthe et al., 2015; Cascini et al., 2015).
(2) Although, near real time daily rainfall data of TRMM cannot replace the rain-gauge data, absence of rain gauges in the study area and highly nonlinear distribution of rainfall in space and time (Martha et al., 2015; Allen et al., 2016; Bhattacharjee et al., 2017) makes the satellite data best viable option.
(3) Ideally, a single 2D profile section in slope stability analysis may not represent the material variability as well as stress and displacement in the landslide slope (Liu et al., 2018). However, considering complex, active and inaccessible (~75° steep slope) nature of the Urni landslide, it was not feasible to determine the slope material properties in spatially varying perspective. Therefore, we have limited our analysis at single representative section (2D).
(4) For simulation of debris flow, we have used Voellmy model (Voellmy, 1955). The model simulates the process by taking source volume into consideration while recent studies have shown that debris flow characteristics are more sensitive to underlying surface conditions (pore water pressure and debris particle) and less to source volume (Yu et al., 2014). This limitation, however, may be compensated by the conservative outcome of the Voellmy rheology in comparison to other available rheology like Friction and Bingham model (Hungr and Evans, 1996).

6. Conclusions

The main outcomes are as follows:

(1) The landslide has attained an areal increase of 103,900 ± 1142 m^2 during the years 2004–2016. About ~86% of this growth occurred since the year 2013. The movement prone '0.80 ± 0.32' million m^3 debris is estimated to be retained by the landslide.
(2) The annual rainfall in the region has increased since the year 2013. About ~42% increase is observed in the mean annual rainfall from 1460 mm/yr (year 2000–2012) to 2075 mm/yr (year 2013–2016). Two extreme rainfall events; 11th June, 2013 (~100 mm) and 16th June, 2013 (~115 mm) are considered to be responsible for the sudden areal increase in the landslide and the partial damming.
(3) The FEM analysis revealed a critical FOS of 1.01, implying unstable tendency. The pattern and order of shear strain (0.00–0.16) and total displacement (0.0–0.6 m) in the slope showed the potential for further movement. Wedge and planar type rock failure are also predicted in the rockmass at the flanks of landslide.
(4) A debris flow of ~25 m/s velocity and ~15 m height is predicted in a preliminary assessment using debris flow simulation. The debris flow is found to spread ~500 m long in the upstream and downstream direction from the landslide location that may destroy nearby bridges (02), NH-05 and Choling village.
(5) At '0.80 ± 0.32' million m^3 landslide volume, potential landslide dam is estimated to attain a maximum height of 76 ± 30 m. Geomorphic indices (MOI, HDSI, and DBI) and grain size analysis indicated instability of this potential landslide dam.

Acknowledgement

The authors are thankful to the Director, Wadia Institute of Himalayan Geology (WIHG) for all the necessary help and support. VK acknowledges Dr. Amit Kumar and Mr. Anupam Anand Gokhale for the affirmative discussion about rainfall dynamics. VK also thank people of Urni and Tapri town, Kinnaur for helpful discussion during field. SLC acknowledges the financial help by the Indian Space Research Organization (ISRO) through TDP project for debris flow modelling. We are thankful to the Editorial Advisor (Prof. M. Santosh), Associate Editor (Prof. Shaji E) and two anonymous reviewers for their constructive suggestions. This study forms a part of the doctoral thesis of VK.

References

Allen, S.K., Rastner, P., Arora, M., Huggel, C., Stoffel, M., 2016. Lake Outburst and debris flow disaster at Kedarnath, June 2013: hydro meteorological triggering and topographic predisposition. Landslides 13 (6), 1479–1491. https://doi.org/10.1007/s10346-015-0584-3.
Barton, N., Bandis, S., 1982. Effects of block size on the shear behavior of jointed rock. In: Proc. 23rd US Symposium on Rock Mechanics. American Rock Mechanics Association, pp. 739–760.
Barton, N., Bandis, S., 1990. In: Barton, N., Stephansson, O. (Eds.), Review of Predictive Capabilities of JRC-JCS Model in Engineering Practice. Rock Joints, Rotterdam, pp. 603–610.
Barton, N., Choubey, V., 1977. The shear strength of rock joints in theory and practice. Rock Mechanics and Rock Engineering 10 (1), 1–54.
Barton, N., 1973. Review of a new shear-strength criterion for rock joints. Engineering Geology 7 (4), 287–332.
Berthelsen, A., 1951. A geological section through the Himalaya. Meddelelser Dansk geologisk forening (Danish). Announcement of Geological Society of Denmark (English) 12, 102–104.
Bhattacharjee, S., Champati Ray, P.K., Chattoraj, S.L., Dhara, M., 2017. Precipitation intensity: Duration based threshold analysis for initiation of landslides in upper Alaknanda valley. International Journal of Environmental Chemical Ecological Geological and Geophysical Engineering 11 (2), 105–109. DOI: scholar.waset.org/1999.34/61982.
Blöthe, J.H., Korup, O., Schwanghart, W., 2015. Large landslides lie low: excess topography in the Himalaya-Karakoram ranges. Geology 43 (6), 523–526. https://doi.org/10.1130/G36527.1.
Bowles, J.E., 1996. Foundation Analysis and Design, fifth ed. McGraw-Hill, New York, p. 750.
Bull, W.B., McFadden, L.D., 1977. Tectonic geomorphology north and south of the Garlock fault, California. Geomorphology in arid regions. In: Proc. 8th Annual Geomorphology Symposium. State University of New York, Binghamton, pp. 115–138.
Cai, M., Kaiser, P.K., Tasaka, Y., Minami, M., 2007. Determination of residual strength parameters of jointed rock masses using the GSI system. International Journal of Rock Mechanics and Mining Sciences 44 (2), 247–265. https://doi.org/10.1016/j.ijrmms.2006.07.005.
Canuti, P., Casagli, N., Ermini, L., 1998. Inventory of landslide dams in the Northern Apennine as a model for induced flood hazard forecasting. In: Andah, K. (Ed.), Managing Hydro-geological Disasters in a Vulnerable Environment for

Sustainable Development. National Research Council of Italy, UNESCO (IHP), Porano, pp. 189–202.
Casagli, N., Ermini, L., Rosati, G., 2003. Determining grain size distribution of the material composing landslide dams in the Northern Apennines: sampling and processing methods. Engineering Geology 69 (1), 83–97. https://doi.org/10.1016/S0013-7952(02)00249-1.
Cascini, L., Ciurleo, M., Di Nocera, S., Gullà, G., 2015. A new–old approach for shallow landslide analysis and susceptibility zoning in fine-grained weathered soils of southern Italy. Geomorphology 241, 371–381. https://doi.org/10.1016/j.geomorph.2015.04.017.
Chandramouli, C., 2011. Census of India 2011. Ministry of Home Affairs. Government of India, New Delhi.
Chattoraj, S.L., Champatiray, P.K., 2015. Simulation and modelling of debris flows using satellite derived data: a case study from Kedarnath area. International Journal of Geomatics and Geosciences 6 (2), 1498–1511.
Costa, J.E., Schuster, R.L., 1988. The formation and failure of natural dams. The Geological Society of America Bulletin 100 (7), 1054–1068.
Costa, J.E., Schuster, R.L., 1991. Documented Historical Landslide Dams from Around the World. U.S. Geological Survey, Vancouver. USGS report no., pp. 91–239.
Cruden, D.M., Varnes, D.J., 1996. Landslide types and processes. In: Turner, A.K., Schuster, R.L. (Eds.), Landslides Investigation and Mitigation (Special Report 247). Transportation Research Board, US National Research Council, Washington.
Dai, F.C., Lee, C.F., Deng, J.H., Tham, L.G., 2005. The 1786 earthquake-triggered landslide dam and subsequent dam-break flood on the Dadu River, southwestern China. Geomorphology 65 (3), 205–221. https://doi.org/10.1016/j.geomorph.2004.08.011.
Deere, D.U., Miller, R.P., 1966. Engineering Classification and Index Properties for Intact Rock. Illinois University at Urbana, USA.
DeGraff, J.V., Rogers, C.T., 2003. An unusual landslide-dam event in Dominica, West Indies. Landslide News 14 (15), 8–11.
Delaney, K.B., Evans, S.G., 2015. The 2000 Yigong landslide (Tibetan Plateau), rockslide-dammed lake and outburst flood: review, remote sensing analysis, and process modelling. Geomorphology 246, 377–393. https://doi.org/10.1016/j.geomorph.2015.06.020.
Dong, J.J., Tung, Y.H., Chen, C.C., Liao, J.J., Pan, Y.W., 2011. Logistic regression model for predicting the failure probability of a landslide dam. Engineering Geology 117 (1), 52–61.
Duman, T.Y., 2009. The largest landslide dam in Turkey: tortum landslide. Engineering Geology 104 (1), 66–79. https://doi.org/10.1016/j.enggeo.2008.08.006.
Dunning, S.A., Armitage, P.J., 2011. The grain-size distribution of rock-avalanche deposits: implications for natural dam stability. In: Evans, S.G., Hermanns, R.L., Strom, A., Scarascia-Mugnozza, G. (Eds.), Natural and Artificial Rockslide Dams. Springer Verlag Berlin Heidelberg, pp. 479–498. https://doi.org/10.1007/978-3-642-04764-0_19.
Eberhardt, E., Stead, D., Coggan, J.S., 2004. Numerical analysis of initiation and progressive failure in natural rock slopes-the 1991 Randa rockslide. International Journal of Rock Mechanics and Mining Sciences 41 (1), 69–87.
Ermini, L., Casagli, N., 2003. Prediction of the behaviour of landslide dams using a geomorphological dimensionless index. Earth Surface Processes and Landforms 28 (1), 31–47.
Evans, S.G., Delaney, K.B., Hermanns, R.L., Strom, A., Scarascia-Mugnozza, G., 2011. The formation and behaviour of natural and artificial rockslide dams; implications for engineering performance and hazard management. In: Evans, S.G., Hermanns, R.L., Strom, A., Scarascia-Mugnozza, G. (Eds.), Natural and Artificial Rockslide Dams. Springer Verlag Berlin Heidelberg, pp. 1–75. https://doi.org/10.1007/978-3-642-04764-0.
Fisher, G.B., Amos, C.B., Bookhagen, B., Burbank, D.W., Godard, V., 2012. Channel widths, landslides, faults, and beyond: the new world order of high-spatial resolution Google Earth imagery in the study of earth surface processes. Geological Society of America Special Papers 492, 1–22. https://doi.org/10.1130/2012.2492 (01).
Folk, R.L., Ward, W.C., 1957. Brazos River bar: a study in the significance of grain size parameters. Journal of Sedimentary Petrology 27, 3–26. https://doi.org/10.1306/74D70646-2B21-11D7-8648000102C1865D.
Fujisawa, K., Kobayashi, A., Aoyama, S., 2009. Theoretical description of embankment erosion owing to overflow. Geotechnique 59 (8), 661–671. https://doi.org/10.1680/geot.7.00035.
Griffiths, D.V., Lane, P.A., 1999. Slope stability analysis by finite elements. Geotechnique 49 (3), 387–403. https://doi.org/10.1680/geot.1999.49.3.387.
Gupta, V., Nautiyal, H., Kumar, V., Jamir, I., Tandon, R.S., 2016b. Landslides hazards around Uttarkashi township, Garhwal Himalaya, after the tragic flash flood in June 2013. Natural Hazards 80, 1689–1707. https://doi.org/10.1007/s11069-015-2048-4.
Gupta, V., Sah, M.P., 2008. Impact of the trans-Himalayan landslide lake outburst flood (LLOF) in the Satluj catchment, Himachal Pradesh, India. Natural Hazards 45 (3), 379–390. https://doi.org/10.1007/s11069-007-9174-6.
Gupta, V., 2005. The relationship between tectonic stresses, joint patterns and landslides. Journal of Nepal Geological Society 31, 51–58. https://doi.org/10.3126/jngs.v31i0.260.
Gupta, V., Bhasin, R.K., Kaynia, A.M., Kumar, V., Saini, A.S., Tandon, R.S., Pabst, T., 2016a. Finite element analysis of failed slope by shear strength reduction technique: a case study for Surabhi Resort Landslide, Mussoorie township, Garhwal Himalaya. Geomatics. Natural Hazards and Risk 7 (5), 1677–1690. https://doi.org/10.1080/19475705.2015.1102778.
Hoek, E., Bray, J.D., 1981. Rock Slope Engineering, third ed. Taylor and Francis, U.K., pp. 150–224
Hoek, E., Carranza-Torres, C., Corkum, B., 2002. Hoek-Brown failure criterion. In: Proc. NARMS-TAC-2002, Toronto, vol. 1, pp. 267–273.
Hogg, R.V., Craig, A.T., 1995. Introduction to Mathematical Statistics, fifth ed. Prentice Hall, New Jersey, pp. 269–278.
Hungr, O., Evans, S.G., 1996. Rock avalanche runout prediction using a dynamic model. In: Proc. 7th International Symposium on Landslides, Trondheim, Norway, vol. 1, pp. 233–238.
Hungr, O., Evans, S.G., 2004. Entrainment of debris in rock avalanches: an analysis of a long run-out mechanism. Geological Society of America Bulletin 116 (9–10), 1240–1252.
IS: 2720 (Part 10), 1991. Method of test for soils: determination of unconfined compressive strength. In: Bureau of Indian Standards, Delhi, India.
IS: 2720 (Part 13), 1986. Method of test for soils: direct shear test. In: Bureau of Indian Standards, New Delhi, India.
IS: 2720 (Part 4), 1985. Methods of test for soils: grain size analysis. In: Bureau of Indian Standards, New Delhi, India.
IS: 9143, 1979. Method for the determination of unconfined compressive strength of rock materials. In: Bureau of Indian Standards, New Delhi, India.
Jamir, I., Gupta, V., Kumar, V., Thong, G.T., 2017. Evaluation of potential surface instability using finite element method in Kharsali Village, Yamuna Valley, Northwest Himalaya. Journal of Mountain Science 14 (8), 1666–1676. https://doi.org/10.1007/s11629-017-4410-3.
Kainthola, A., Singh, P.K., Singh, T.N., 2015. Stability investigation of road cut slope in basaltic rockmass, Mahabaleshwar, India. Geoscience Frontiers 6 (6), 837–845. https://doi.org/10.1016/j.gsf.2014.03.002.
Keller, E.A., Pinter, N., 2002. Active Tectonics: Earthquakes, Uplift, and Landscape, second ed. Prentice Hall, New Jersey.
Korup, O., 2004. Geomorphometric characteristics of New Zealand landslide dams. Engineering Geology 73 (1), 13–35. https://doi.org/10.1016/j.enggeo.2003.11.003.
Kumar, A., Asthana, A.K.L., Priyanka, R.S., Jayangondaperumal, R., Gupta, A.K., Bhakuni, S.S., 2017. Assessment of landslide hazards induced by extreme rainfall event in Jammu and Kashmir Himalaya, northwest India. Geomorphology 284, 72–87.
Kumar, V., Gupta, V., Jamir, I., 2018a. Hazard evaluation of progressive Pawari landslide zone, Satluj valley, Himachal Pradesh, India. Natural Hazards 1–19.
Kumar, V., Gupta, V., Sundriyal, Y.P., 2018b. Spatial interrelationship of landslides, litho-tectonics, and climate regime, Satluj valley, Northwest Himalaya. Geological Journal. https://doi.org/10.1002/gj.3204.
Larsen, M.C., Wieczorek, G.F., 2006. Geomorphic effects of large debris flows and flash floods, northern Venezuela, 1999. Zeitschrift fur Geomorphologie 145, 147–175.
Li, T., Schuster, R.L., Wu, J., 1986. Landslide dams in south-central China. In: Proc. Landslide Dams: Processes, Risk, and Mitigation. ASCE Convention, Washington, pp. 146–162.
Liu, Y., Zhang, W., Zhang, L., Zhu, Z., Hu, J., Wei, H., 2018. Probabilistic stability analyses of undrained slopes by 3D random fields and finite element methods. Geoscience Frontiers 9 (6), 1657–1664. https://doi.org/10.1016/j.gsf.2017.09.003.
Marinos, V., Marinos, P., Hoek, E., 2005. The geological strength index: applications and limitations. Bulletin of Engineering Geology and the Environment 64 (1), 55–65. https://doi.org/10.1007/s10064-004-0270-5.
Martha, T.R., Roy, P., Govindharaj, K.B., Kumar, K.V., Diwakar, P.G., Dadhwal, V.K., 2015. Landslides triggered by the June 2013 extreme rainfall event in parts of Uttarakhand state, India. Landslides 12 (1), 135–146. https://doi.org/10.1007/s10346-014-0540-7.
Matsui, T., San, K.C., 1992. Finite element slope stability analysis by shear strength reduction technique. Soils and Foundations 32 (1), 59–70.
Mohammed, N.Z., Ghazi, A., Mustafa, H.E., 2013. Positional accuracy testing of Google earth. International Journal of Multidisciplinary Sciences and Engineering 4 (6), 6–9.
Pain, A., Kanungo, D.P., Sarkar, S., 2014. Rock slope stability assessment using finite element based modelling—examples from the Indian Himalayas. Geomechanics and Geoengineering 9 (3), 215–230. https://doi.org/10.1080/17486025.2014.883465.
Parvaiz, I., Champatiray, P.K., Bhat, F.A., Dadhwal, V.K., 2012. Earthquake-induced landslide dam in the kashmir himalayas. International Journal of Remote Sensing 33 (2), 655–660. https://doi.org/10.1080/01431161.2010.512948.
Ray, P.C., Chattoraj, S.L., Bisht, M.P.S., Kannaujiya, S., Pandey, K., Goswami, A., 2016. Kedarnath disaster 2013: causes and consequences using remote sensing inputs. Natural Hazards 81 (1), 227–243. https://doi.org/10.1007/s11069-015-2076-0.
Ruiz-Villanueva, V., Allen, S., Arora, M., Goel, N.K., Stoffel, M., 2016. Recent catastrophic landslide lake outburst floods in the Himalayan mountain range. Progress in Physical Geography 41 (1), 3–28. https://doi.org/10.1177/0309133316658614.
Sajinkumar, K.S., Asokakumar, M.R., Sajeev, R., Venkatraman, N.V., 2017. A potential headward retreat landslide site at Munnar, Kerala. Journal of the Geological Society of India 89 (2), 183–191. https://doi.org/10.1007/s12594-017-0582-2.
Schwanghart, W., Worni, R., Huggel, C., Stoffel, M., Korup, O., 2016. Uncertainty in the Himalayan energy–water nexus: estimating regional exposure to glacial lake outburst floods. Environmental Research Letters 11 (7), 074005. https://doi.org/10.1088/1748-9326/11/7/074005.
Sharma, K.K., 1977. A contribution to the geology of Satluj valley, Kinnaur, Himachal Pradesh, India. In: Proc. CNRS International Symposiums, vol. 268, pp. 369–378.
Sharma, S., Shukla, A.D., Bartarya, S.K., Marh, B.S., Juyal, N., 2017. The Holocene floods and their affinity to climatic variability in the western Himalaya, India. Geomorphology 290, 317–334.

Singh, P., Ramanathan, A.S., Ghanekar, V.G., 1974. Flash floods in India. International Association of Hydrological Science 112, 114–118.
Sosio, R., Crosta, G.B., Hungr, O., 2008. Complete dynamic modelling calibration for the Thurwieser rock avalanche (Italian Central Alps). Engineering Geology 100 (1), 11–26.
Srikantia, S.V., Bhargava, O.N., 1998. Geology of Himachal Pradesh. Geological Survey of India, Bangalore, India.
Stefanelli, C.T., Segoni, S., Casagli, N., Catani, F., 2016. Geomorphic indexing of landslide dams evolution. Engineering Geology 208, 1–10. https://doi.org/10.1016/j.enggeo.2016.04.024.
Sundriyal, Y.P., Tripathi, J.K., Sati, S.P., Rawat, G.S., Srivastava, P., 2007. Landslide-dammed lakes in the Alaknanda basin, lesser Himalaya: causes and implications. Current Science 93 (4), 568.
Swanson, F.J., Oyagi, N., Tominaga, M., 1986. Landslide dams in Japan. In: Proc. Landslide Dams: Processes, Risk, and Mitigation. ASCE convention, Washington, pp. 131–145.
Takahashi, T., Nakagawa, H., 1993. Flood and debris flow hydrograph due to collapse of a natural dam by overtopping. In: Proc. Hydraulic Engineering, Japan, vol. 37, pp. 699–704. https://doi.org/10.2208/prohe.37.699.
Thiede, R.C., Ehlers, T.A., Bookhagen, B., Strecker, M.R., 2009. Erosional variability along the northwest Himalaya. Journal of Geophysical Research Earth Surface 114, F01015. https://doi.org/10.1029/2008JF001010.
Vannay, J.C., Grasemann, B., Rahn, M., Frank, W., Carter, A., Baudraz, V., Cosca, M., 2004. Miocene to Holocene exhumation of metamorphic crustal wedges in the NW Himalaya: evidence for tectonic extrusion coupled to fluvial erosion. Tectonics 23 (1), 1–24. https://doi.org/10.1029/2002TC001429.
Voellmy, A., 1955. Uber die Zerstorungskraft von Lawmen. Schweizerische Bauzeitung, vol. 73, no. 12, 15, 17, 19, 37. On the destructive force of avalanches, Translation No. 2. Alta. Avalanche Study Center, USDA, Forest Service, p. 1964.
Wang, G., Furuya, G., Zhang, F., Doi, I., Watanabe, N., Wakai, A., Marui, H., 2016. Layered internal structure and breaching risk assessment of the Higashi-Takezawa landslide dam in Niigata, Japan. Geomorphology 267, 48–58. https://doi.org/10.1016/j.geomorph.2016.05.021.
Wulf, H., Bookhagen, B., Scherler, D., 2010. Seasonal precipitation gradients and their impact on fluvial sediment flux in the Northwest Himalaya. Geomorphology 118 (1), 13–21. https://doi.org/10.1016/j.geomorph.2009.12.003.
Xu, Q., Chen, J., Li, J., Zhao, C., Yuan, C., 2015. Study on the constitutive model for jointed rock mass. PLoS One 10 (4), e0121850. https://doi.org/10.1371/journal.pone.0121850.
Yu, G., Zhang, M., Chen, H., 2014. The dynamic process and sensitivity analysis for debris flow. In: Sassa, K., Canuti, P., Yin, Y. (Eds.), Landslide Science for a Safer Geoenvironment. Springer. https://doi.org/10.1007/978-3-319-05050-8_26.
Zienkiewicz, O.C., Humpheson, C., Lewis, R.W., 1975. Associated and non-associated visco-plasticity and plasticity in soil mechanics. Geotechnique 25 (4), 671–689.